Assessment of RANS Based CFD Methodology using JAEA Experiment with a Wire-wrapped 127-pin Fuel Assembly

J. H. Jeong [a*], J. Yoo [a], K. L. Lee [a], K. S. Ha [a]
[a] *Korea Atomic Energy Research Institute, 989-111, Daedeok-daero, Yuseong-gu, Daejeon, 305-353*
[*] *Corresponding author: jhjeong@kaeri.re.kr*

1. Introduction

The SFR (Sodium-cooled Fast Reactor) system is one of the nuclear reactors in which a recycling of transuranics (TRUs) by reusing spent nuclear fuel sustains the fission chain reaction. This situation strongly motivated the Korea Atomic Energy Research Institute (KAERI) to start a prototype Gen-Ⅳ Sodium-cooled Fast Reactor (PGSFR) design project under the national nuclear R&D program. Generally, the SFR system has a tight package of the fuel bundle and a high power density. The sodium material has a high thermal conductivity and boiling temperature than the water. That can make core design to be more compact than Light Water Reactor (LWR) through narrower sub-channels. The fuel assembly of the SFR system consists of long and thin wire-wrapped fuel bundles and a hexagonal duct, in which wire-wrapped fuel bundles in the hexagonal tube has triangular loose array. The main purpose of a wire spacer is to avoid collisions between adjacent rods. Furthermore, a wire spacer can mitigate a vortex induced vibration, and enhance convective heat transfer due to the secondary flow by helical type wire spacers.

Most of numerical studies in the nuclear fields was widely conducted based on the simplified sub-channel analysis codes such as COBRA (Rowe [1]), SABRE (Macdougall and Lillington [2]), ASFRE (Ninokata [3]), and MATRA-LMR (Kim et al. [4]). The sub-channel analysis codes calculate the temperature, pressure, and velocity value averaged in a sub-channel, which is the fully mixed state of flow field in a sub-channel.

Recently, a huge increase of computer power allow to three-dimensional simulation of thermal hydraulics of wire-wrapped fuel bundles. The applicability of RANS approaches has already been assessed by Pointer et al. [5]. Amad et al. [6], Gajapathy et al. [7] performed the three-dimensional flow and heat transfer analysis by using the RANS based simulation. Raza et al. [8] investigated three kinds of cross sectional shapes of wire spacer, circle, hexagon, and rhombus by using the RANS based simulation. The overall pressure drop was highest in case of rhombus shaped wire spacer. Pointer et al. [9-10] and Fischer et al. [11] implemented the comparison of LES and RANS results in the 7-pin fuel assembly test section. The comparison of both sub-channel mixing velocity provide some confidence that RANS-based simulation can be expected to provide acceptably accurate hydrodynamic prediction. Based on their studies, RANS simulation tends to predict more inter-channel mixing. Jeong et al. [12] has presented a possible path for the RANS based CFD methodology applicable to real scale 217-pin wire-wrapped fuel assembly of KAERI PGSFR [12].

In this paper, we assess the RANS based CFD methodology with JAEA experimental data [13]. The JAEA experiment study with the 127-pin wire-wrapped fuel assembly was implemented using water for validating pressure drop formulas in ASFRE code. Complicated and vortical flow phenomena in the wire-wrapped fuel bundles were captured by vortex structure identification technique based on the critical point theory. Furthermore, the relationship between complex flow phenomena and helically wrapped-wire spacers will be discussed.

2. Numerical Analysis Methodology

2.1 Test Section

A numerical study of the 127-pin fuel assembly was carried out in JAEA Oarai engineering center. The geometric parameters of the 127-pin fuel assembly are summarized in Table 1 [13]. Figure 1 shows a schematic of the test section of the fuel assembly with wire spacers. As shown in Table 1 and Fig. 1, the wire-wrapped 127-pin bundle was centered in a hexagonal duct, with a 74.7 mm flat-to-flat distance inside. The pins were 5.5 mm in diameter, arranged in a triangular array with a pin pitch of 6.47 mm. The pitch-to-diameter ratio (P/D) was 1.176. The 127 pins of 6.5 mm in diameter were wrapped by wire spacers of 0.9 mm in diameter with a wrapping lead of 293.9 mm.

Table 1. Test section geometric parameters of wire-wrapped 127-pin fuel assembly

Geometric parameters	Value
Number of pins	127
Pin diameter (mm)	5.5
Pin pitch (mm)	6.47
Pitch-to diameter ratio	1.176
Pin length (mm)	1172
Duct inner flat-to-flat distance (mm)	74.7
Wire spacer diameter (mm)	0.9
Wire lead pitch (mm)	293.9

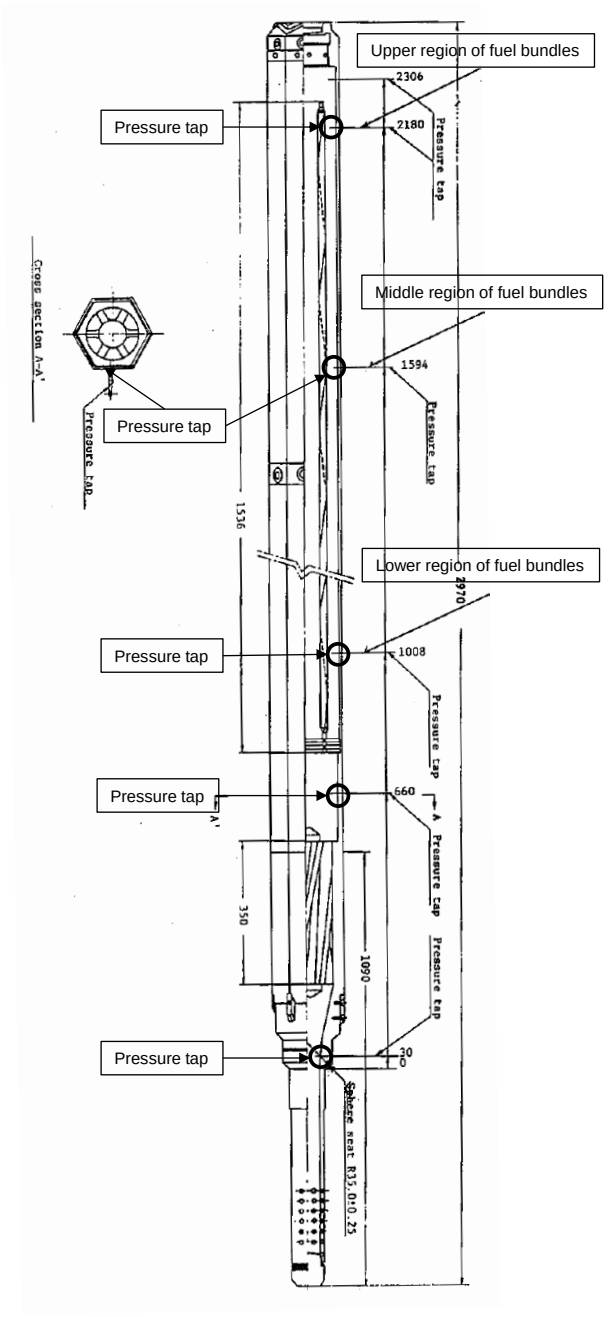

(a) Side view

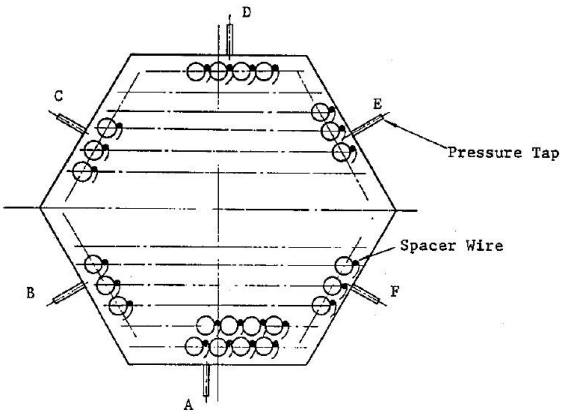

(b) Cross sectional view

Fig. 1. Test section of 127-pin fuel assembly [13]

As shown in Fig. 1, pressure tap on the duct wall has been embedded to measure axial pressure distribution and circumferential pressure distribution. Table 2 depicts the experimental conditions of test cases with water.

Table 2. Test cases of wall pressure measurement

Case	1	2	3	4	5
Water temperature [K]	348.15	348.15	348.15	348.15	348.15
Density [kg/m^3]	974.63	974.63	974.63	974.63	974.63
Mass flow-rate [kg/s]	11.614	8.961	6.254	18.613	5.076
Reynolds Number	43760	33764	23563	70129	19126

2.2 Test Section of Numerical Analysis

The present CFD investigation was carried out over the full-scale experimental facility of JAEA's 127-pin fuel assembly. Figure 2 shows the test section of the numerical analysis. As shown in perspective view of Fig. 2, total length of numerical analysis is defined to be the same as full scale of test section in Fig. 1 (a). The helically wrapped 127 wire spacers are also fully modeled in numerical analysis of Fig. 2.

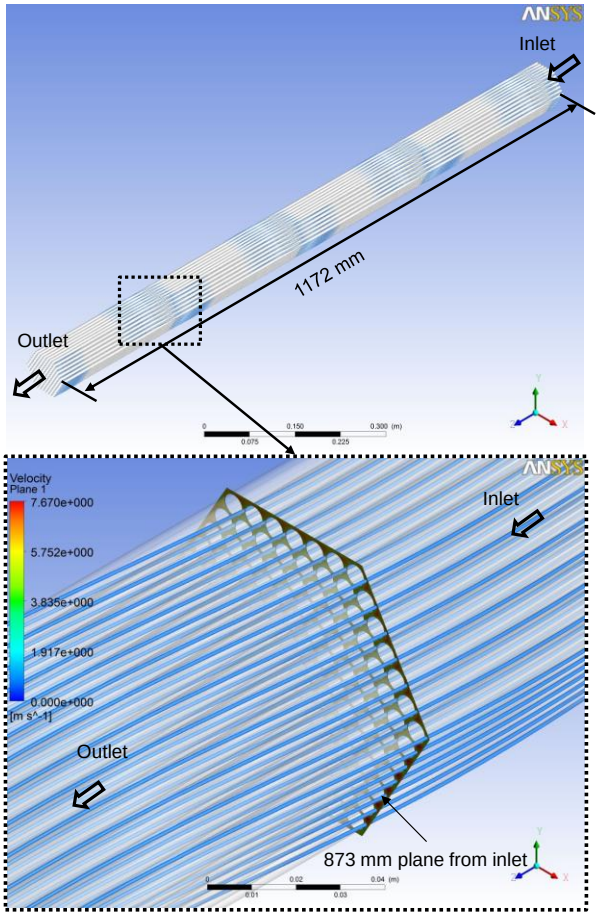

Fig. 2. Test section of numerical analysis

2.3 Computational Grids and Boundary Conditions

Figure 3 shows the cross sectional view with grid distribution, which is divided into an inner fluid and an outer fluid by a boundary line with green color. The green dotted lines in Fig. 3 is the patches nodes on each side of the interface of the helically arranged meshes (inner fluid region) and straightly arranged meshes (outer fluid region) in the stream-wise direction. As shown in Fig. 3, computational grid systems of the 127-pin fuel assembly are composed of hexagonal meshes.

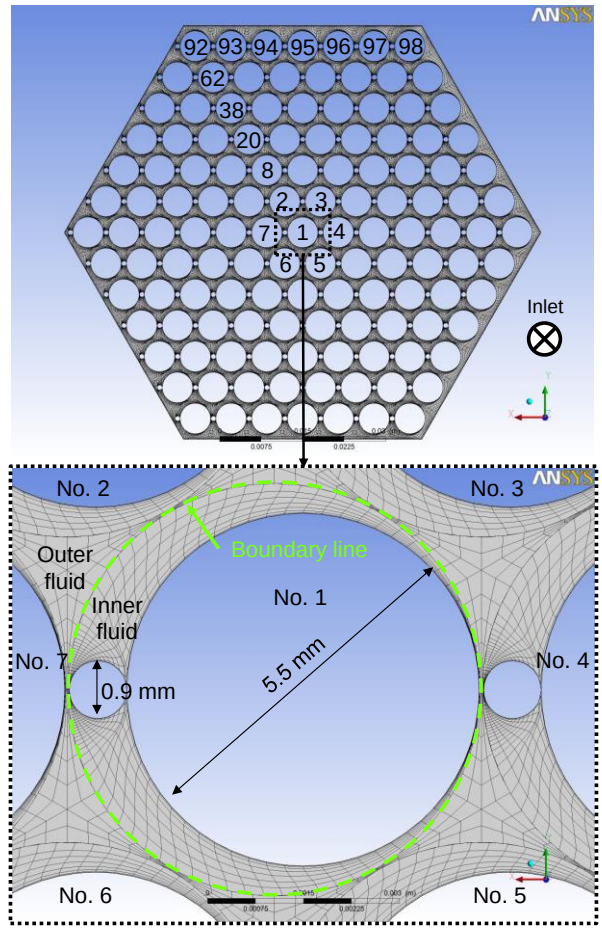

Fig. 3. Cross sectional view with grid distribution

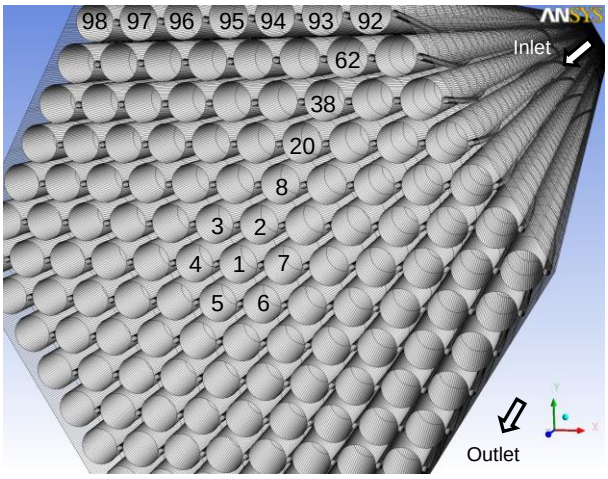

Fig. 4. Perspective view with axial grid distribution

All fuel bundles are numbered 1 through 127 clockwise. Figure 4 shows the perspective view with axial grid distribution. Compared to other studies [5-11] with a trimmed shape at the interface between pin surface and wire surface, this RANS based flow simulation is carried out without any trimmed shapes.

Table 3 describes the computational grids system. The computational grid system is divided into two regions: the inner fluid and the outer fluid part. The total number of computational grids in the system was approx. 1.61×10^7 cells.

Table 3. Computational grid system

127-Pin	Cells	Nodes	Elements
Inner fluid	13,373,100	13,901,171	13,373,100
Outer fluid	2,681,640	4,263,631	2,681,640
Total	16,054,740	18,164,802	16,054,740

Table 4 describes the computational boundary condition of the CFD analysis. The inlet and outlet are defined with various mass flow-rate with temperature of 343.15 K, and a relative pressure of 0 Pa, respectively. The surface of rods and wire spacers is defined with no slip condition with smooth roughness. The duct wall is also applied under no slip condition with smooth roughness.

Table 4. Boundary condition in the 127-pin fuel assembly

Boundary domain	Condition	Value
-Inlet	-Constant mass flow-rate [kg/s]	11.614 8.961 6.254 18.613 5.076
-Outlet	-Relative pressure [Pa]	0
-Rod & wire surface	-No slip (Smooth wall)	-
-Duct Wall	-No slip (Smooth wall)	-

2.4 Turbulence Model

Three major numerical analysis techniques can be used for turbulent flow fields: DNS (Direct Numerical Simulation), LES (Large Eddy Simulation), and RANS (Reynolds-averaged Navier-Stokes) simulation. In order to precisely analyze the general vortex behavior in a turbulent flow field containing vortices of various scales, it is necessary to make the calculation grid size smaller than the minimum space scale of the vortex structure and the time interval less than the minimum time scale of the vortex variation. Assuming that computing the cost of the RANS is equal to one, that of the DNS and LES increases as the cube and square of the Reynolds number, respectively. The Reynolds number based on the averaged axial velocity and the hydraulic diameter of the present fuel assembly is higher than 1.91×10^4. For this reason, the DNS and LES are not feasible

methods for the full-scale 127-pin fuel assembly of the test section. RANS is a very practical and affordable engineering solution with good knowledge of the turbulence.

The turbulence models for the RANS equations are for computing the Reynolds stresses tensor from turbulent fluctuations in the fluid momentum. Turbulence models such as the *k-ε*, *k-w*, and SST have become industry standard models and are commonly used for most types of engineering problems, although the *k-ε* model has the weakness in cases of large adverse pressure gradient, and the *k-w* model is too sensitive to the inlet free-stream turbulence properties (Wilcox et al. [14]). The SST model solves the above problems for switching to the *k-ε* model in the free-stream and the *k-w* model in the viscous sub-layer (Menter et al. [15]). The minimum grid scale on the fuel rod surface was 5.0×10^{-7} mm to capture the laminar to turbulent flow transition with the SST turbulence model; the friction velocity y+ is approximately close to 1.

In the present study, we conducted the steady RANS simulation with the SST turbulence model for investigating the three-dimensional and vortical flow phenomena. The high-resolution scheme was used for the convective term. Convergence of the simulation was judged by the periodic pressure and temperature on the outlet domain of the 127-pin fuel assembly.

3. Numerical Analysis Results

3.1 Comparison of Pressure Drop Correlations

Friction factor correlations such as the Rehme model [16], Engel et al. model [17], and Cheng and Todreas simplified model [18] have been widely used for the wire-wrapped fuel bundle. Each friction factor is calculated through the following correlations.

- Rehme model

$$f = \frac{64}{\mathrm{Re}} \cdot F^{0.5} + \frac{0.0816}{\mathrm{Re}^{0.1333}} \cdot \frac{N_r \cdot \pi \cdot D_r + D_w}{S_t} \tag{1}$$

- Engel, Markley and Bishop model

$$\begin{aligned} &\text{Laminar flow: } f = \frac{110}{\mathrm{Re}} \quad \text{for } \mathrm{Re} \le 400, \\ &\text{Turbulent flow: } f = \frac{0.55}{\mathrm{Re}^{0.25}} \quad \text{for } \mathrm{Re} \ge 5000, \\ &\text{Transition flow: } f = \frac{110}{\mathrm{Re}} \cdot (1-\psi)^{0.5} + \frac{0.55}{\mathrm{Re}^{0.25}} \cdot \psi^{0.5} \\ &\qquad\qquad \text{for } 400 \le \mathrm{Re} \le 5000, \end{aligned} \tag{2}$$

- Cheng and Todreas simplified model

$$\begin{aligned} &\text{Laminar flow: } f = \frac{C_{fL}}{\mathrm{Re}} \quad \text{for } \mathrm{Re} \le \mathrm{Re}_L, \\ &\text{Turbulent flow: } f = \frac{C_{fT}}{\mathrm{Re}^{0.18}} \quad \text{for } \mathrm{Re}_T \le \mathrm{Re}, \\ &\text{Transition flow: } f = \frac{C_{fL}}{\mathrm{Re}} \cdot (1-\psi)^{1/3} + \frac{C_{fT}}{\mathrm{Re}^{0.18}} \cdot \psi^{1/3} \\ &\qquad\qquad \text{for } \mathrm{Re}_L \le \mathrm{Re} \le \mathrm{Re}_T, \end{aligned} \tag{3}$$

where all of the various symbols are defined in the nomenclature section of this paper.

Figure 5 depicts a comparison of the CFD analysis results, JAEA experimental data, and friction factor correlations of the Rehme model, Engel et al. model, and Cheng and Todreas simplified model in various ranges of Reynolds number. As shown in Fig. 7, the CFD analysis results are very close to experimental data. Furthermore, the Rehme model and Cheng and Todreas model have a good agreement with experimental data. The friction factor near the inlet region is also over-estimated until the inlet flow reaches about the end position of one or two periodical wire lead pitch [12]. To calculate the friction factor without numerical boundary effect of inlet region, at least two periodical wire lead pitches should be modeled in the CFD simulation to prevent an over-estimation of the friction factor.

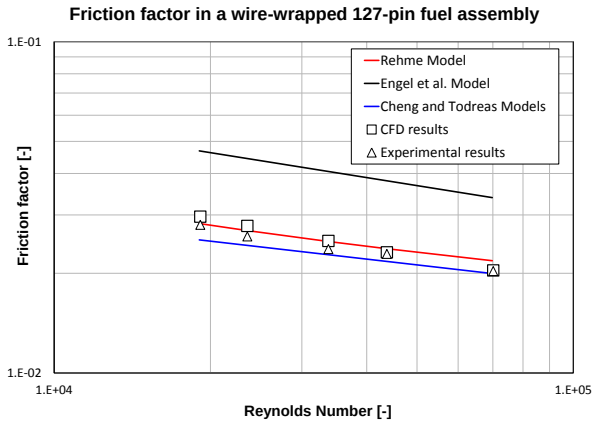

Fig. 5. Comparison of the CFD results with friction factor correlations in various range of Reynolds number

3.2 Complex Flow Behaviors

A three-dimensional and vortical flow field at a Reynolds number of 4.38×10^4 is investigated in this chapter. Figure 6 shows the projected streamline on the cross sectional planes of 735 mm, 808 mm, 881 mm,

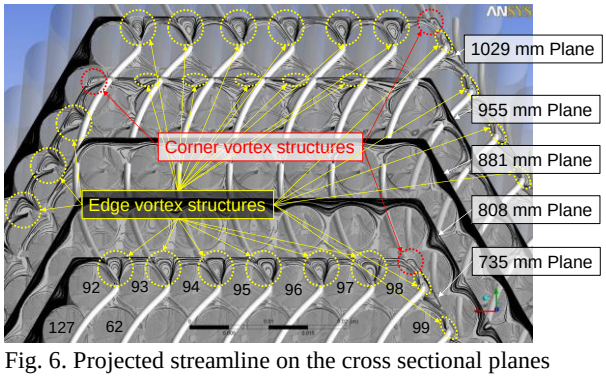

Fig. 6. Projected streamline on the cross sectional planes

955 mm, and 1029 mm, which are corresponding to the relative angular position of −180 deg, −90 deg, 0 deg, 90 deg, and 180 deg between the pin and wire center position. As shown in Fig. 6, the multi-scale vortex structures are developed in the fuel assembly. The vortical and separated flow field is composed of edge vortex structures (yellow dot-line) in the edge sub-channels, corner vortex structures (red dot-line) in the corner sub-channels. The location of the edge and corner vortex structures is closely related with the relative position between the wire and duct wall. As shown in Fig. 6, the edge and corner vortex structures are formed in the tangential direction when the distance from the wire is far from the duct wall.

Figure 7 shows the axial velocity distribution on the cross sectional planes of 735 mm, 808mm, 881 mm, 955 mm, and 1029 mm, which is normalized by the inlet velocity. Regardless of the large-scale vortex structures in the edge sub-channels in Fig. 6, the edge sub-channels have axially higher velocity than the corner and interior sub-channels. This means that axial blockage effect due to the vortex structures does not occur in the edge sub-channels, however, the corner vortex structures partially induce the axial blockage. Wake regions due to helically wrapped wire spacers are locally developed nearby the suction surface of wire spacers, where are located in counter-clockwise position of wire spacers from upstream in Fig. 7. These strong longitudinal vortex structures in the edge sub-channels can achieve better heat transfer characteristics than that in the corner and interior sub-channels [19]. However, corner vortex and wake structures with a low axial velocity suppress heat transfer from fuel clad to coolant.

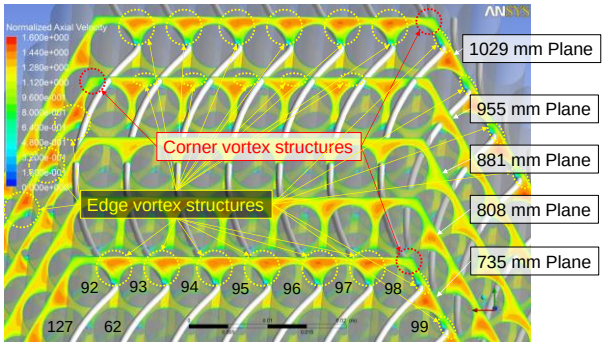

Fig. 7. Normalized axial velocity distribution

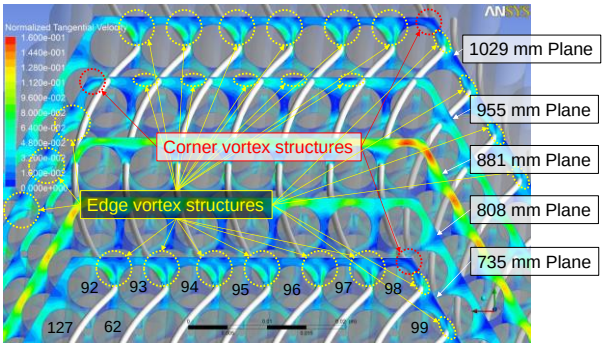

Fig. 8. Normalized axial velocity distribution

Figure 8 shows the tangential velocity distribution on the cross sectional planes of 735 mm, 808mm, 881 mm, 955 mm, and 1029 mm, which is normalized by the inlet velocity. The wire spacers induce a secondary flow by up to about 16 % of the axial velocity magnitude. The secondary flow in the edge and corner sub-channels is periodically much stronger than that in the interior sub-channel in Fig. 8.

Figure 9 shows the turbulent intensity distribution on the cross sectional planes of 735 mm, 808mm, 881 mm, 955 mm, and 1029 mm, which is calculated by the turbulent kinetic energy and inlet velocity. As shown in Fig. 9, the edge sub-channel with strong edge vortex structures has higher turbulence intensity than that without strong edge vortex structure. The turbulence intensity of the edge vortex structures is stronger than that of the corner vortex structure and wake regions adjacent wire spacers. Furthermore, the turbulence intensity with wakes is higher than that with corner vortex structures. Regardless of the vortex behavior in interior sub-channel, the interior sub-channels have the lowest turbulence intensity in fuel assembly.

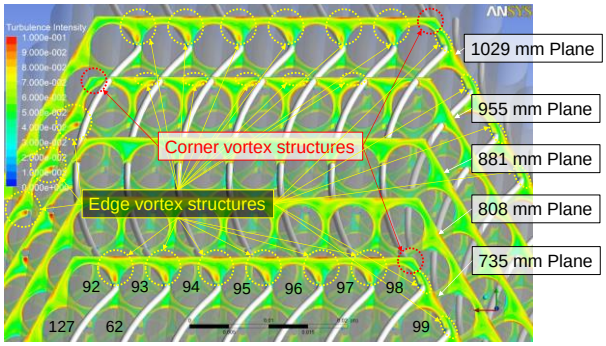

Fig. 9. Turbulence intensity distribution

Figure 10 shows the vorticity distribution on the cross sectional planes of 735 mm, 808mm, 881 mm, 955 mm, and 1029 mm. The edge sub-channel with strong edge vortex structures has higher vorticity than that without strong edge vortex structure. The strength of vorticity with strong edge vortex structures is almost the same as that with the corner vortex structure. However, the vorticity in wake regions is remarkably higher than that in the edge and corner sub-channel with vortex structures.

3.3 Driving Forces on Wire-spacers

The behavior of the secondary flow in the edge, corner, and interior sub-channels is investigated by an assessment of the driving force calculated by the pressure on the wire-spacer wall surface. An analysis of the wire-spacer effect in the fuel assembly was implemented at a Reynolds number of 4.38×10^4.

Figure 11 shows the pressure distribution and limiting streamline on the No. 92 wire-spacer surface of 875 mm ~ 975 mm height. Fig. 11 (a) and (b) are the pressure surface and suction surface, respectively. As shown in

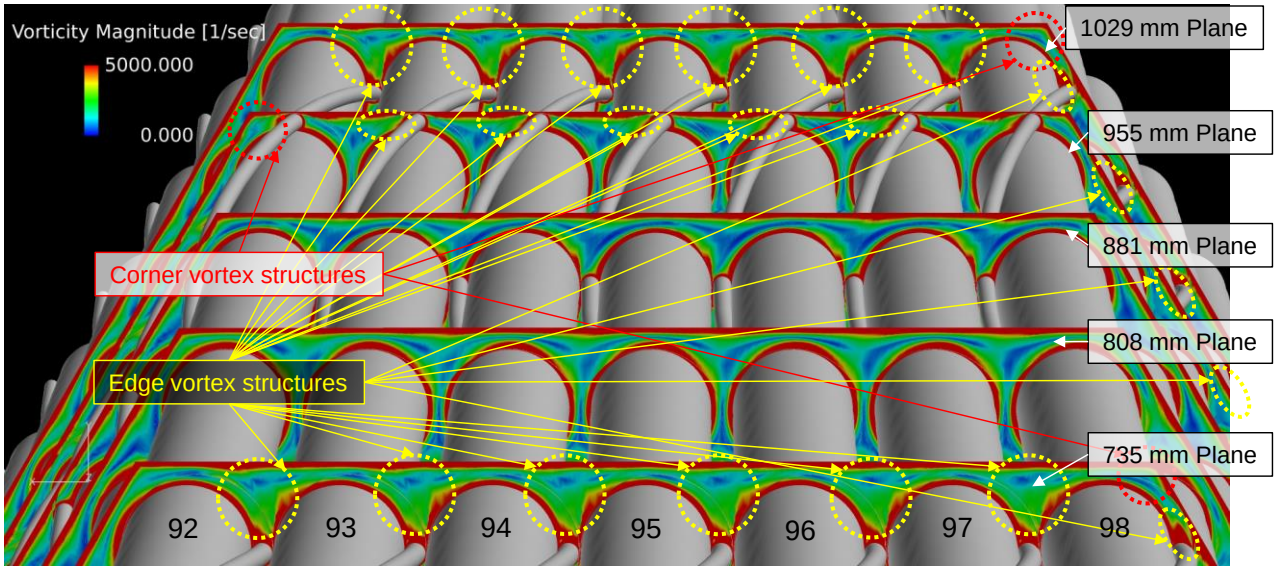

Fig. 10. Vorticity distribution

Fig. 11 (a), the attachment line due to stagnation of the flow is induced at the center of the pressure surface. As shown in Fig. 11 (b), the separation line is formed at the center of the suction surface. However, the separation

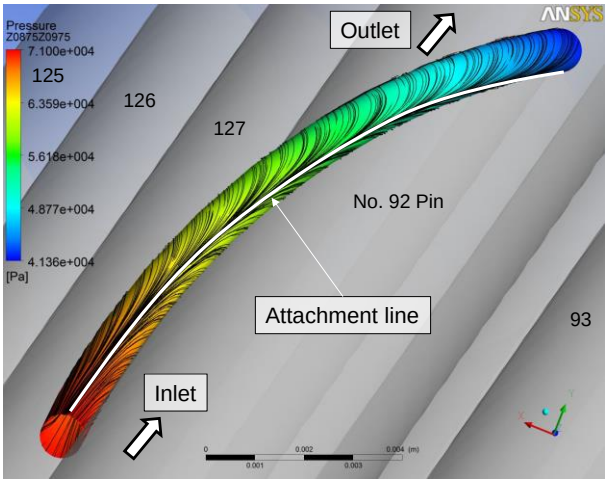

(a) Pressure surface of wire-spacer

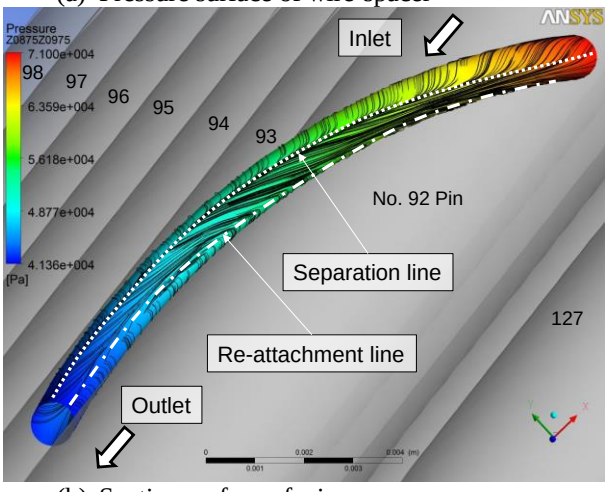

(b) Suction surface of wire-spacer

Fig. 11. Pressure distribution and limiting streamline on the No. 92 wire-spacer surface at 875 mm to 975 mm height

vortex induced by the wire-spacer re-attaches nearby the contacting position of the rod and wire. This re-attachment line was generated by interacting between the secondary flow in the clock-wise direction and the separation vortex due to wire-spacer in the counter clock-wise direction. The interacting position of the suction surface has higher vortcity than the pressure surface.

Figure 12 shows a schematic of the driving forces on the wire-spacer surface of 10 mm axial length, which is corresponding to angular length of 12.3 deg. As shown in Fig. 12, the driving force due to the secondary flow is the forces in the X and Y direction. The drag forced against the axial direction is the Z direction.

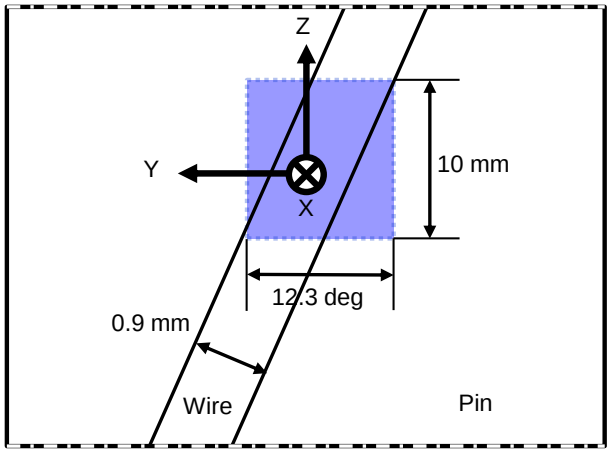

Fig. 12. Schematic of the driving forces on the wire-spacer surface of 10 mm axial length

The driving forces on the wire-spacer surfaces are normalized by the dynamic pressure of the inlet region. The driving forces on the wire surface of 10 mm are defined as Eq. (4).

$$F_{n,10mm} = \frac{F_{10mm}}{0.5 \cdot \rho \cdot U_{in}^2 \cdot D_w \cdot \pi \cdot D_r / N} \quad (4)$$

where all of the various symbols are defined in the nomenclature section of this paper.

Figures 13 and 14 show the normalized driving forces on the wire-spacer surface of 10 mm axial length with different angular position. The angular position on the cross sectional coordinate (X-axis, Y-axis) is defined as Eq. (5).

$$A = \tan^{-1} \frac{Y_{\text{center of wire}} - Y_{\text{center of rod}}}{X_{\text{center of wire}} - X_{\text{center of rod}}} \quad (5)$$

where all of the various symbols are defined in the nomenclature section of this paper.

Figs. 13 (a), (b), and (c) describe the normalized driving forces on the No. 1, 2, 8, 20, 38, 62, and 92 wire-spacers in the X-, Y-, and Z-directions, respectively. As shown in Fig. 13, the behavior of the driving forces on the wire-spacers is remarkably dependent on the angular position of the wire and the rod position and the radial position of the rod in the hexagonal duct. The maximum difference of the driving forces in the X- and Y-directions between the number 1 and 92 rod is under 25 % over the various angular position of wire. The driving forces in the Z- direction of the number 92 rod is about 40% higher than that of the number 1 rod over the various angular position of

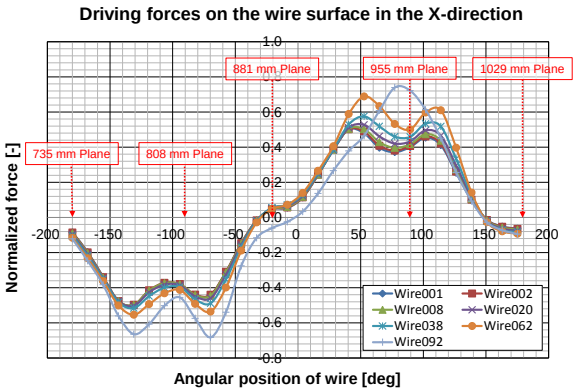

(a) Driving force in the X-direction

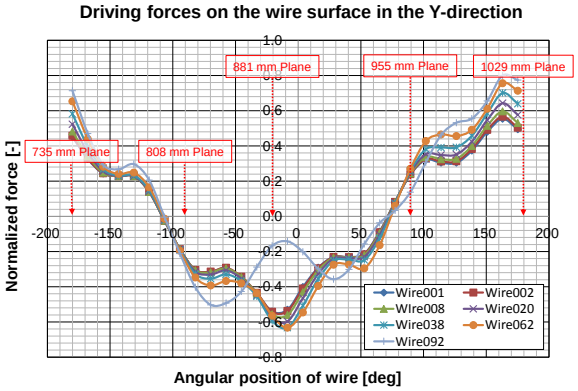

(b) Driving force in the Y-direction

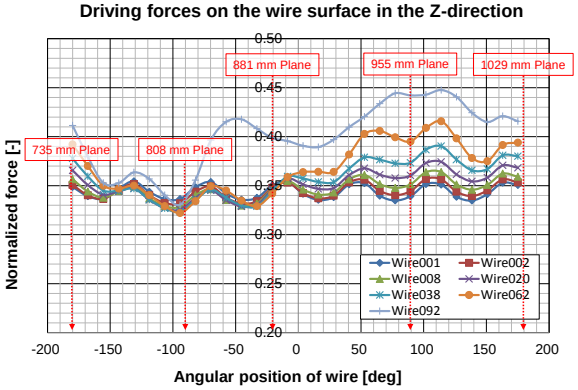

(c) Driving force in the Z-direction

Fig. 13. Normalized driving forces on the No. 1, 2, 8, 20, 38, 62, and 92 wire-spacers

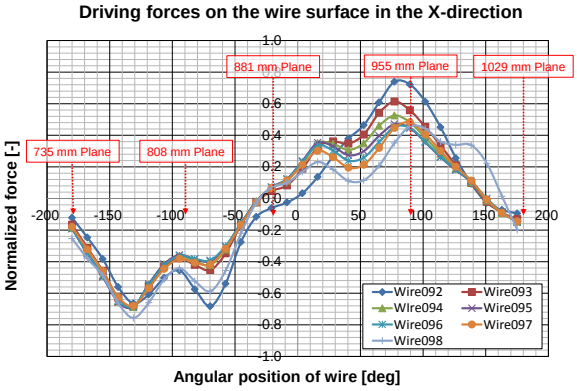

(a) Driving force in the X-direction

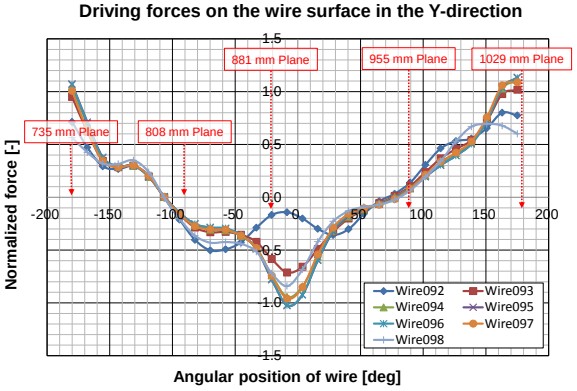

(b) Driving force in the Y-direction

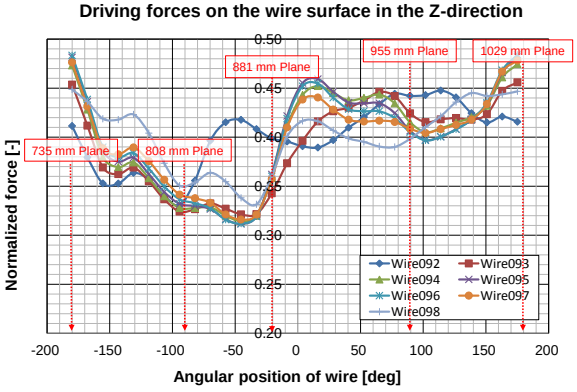

(c) Driving force in the Z-direction

Fig. 14. Normalized driving forces on the No. 92, 93, 94, 95, 96, 97, and 98 wire-spacers

wire-spacer. Axially higher velocity in the edge sub-channels in Fig. 7 makes higher driving forces in X-, Y-, and Z- direction.

Based on the normalized driving forces on the No. 1, 2, 8, 20, 38, 62, and 92 wire-spacers, the driving forces in the Z-direction is remarkably dominated by the radial position in the hexagonal duct than those in the X-, Y-directions. Furthermore, compared with the behavior of the driving forces on the No. 1, 2, 8, 20, 38, and 62 wire-spacers, the interaction on the No. 92 wire-spacer between the wire-spacer and the duct wall generates the different behavior of the driving forces at 40 ~ 120 deg in the X-direction, and at −50 ~ 50 deg in the Y-direction.

Figures 14 (a), (b), and (c) describe the normalized driving forces on the No. 92, 93, 94, 95, 96, 97, and 98 wire-spacers in the X, Y, and Z direction, respectively. As shown in Fig. 14, the behavior of the driving forces on the wire-spacers are dominated by not only the angular position, but also the relative position of the wire and the hexagonal duct wall. For this reason, No. 92 and 98 wire-spacers have the different behavior of the driving forces in a certain angular position, compared with the others.

Figures 15 (a) and (b) describe the normalized X-, Y-, Z-forces on the wire spacer of 1 wire lead pitch in the radial and tangential directions, respectively. As shown in Fig. 15 (a), the Z-driving force on the No. 92 wire-spacer is about 20 % higher than that on the No. 1 wire spacer. As the radial position of the wire-spacer is far away from the No. 1 wire-spacer, there is higher axial velocity, so that driving forces in the X-, Y-, and Z-directions increase. However, when wire-spacers are located in the same radial position and different tangential position, maximum deviation of the X-, Y-, and Z- driving forces was under 6.8 %, 8.0 %, and 2.9 %, respectively.

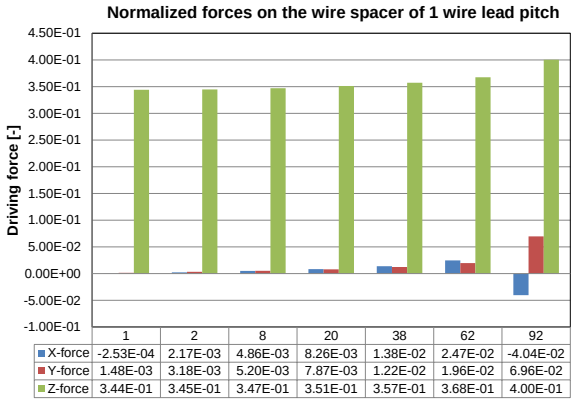

	1	2	8	20	38	62	92
X-force	-2.53E-04	2.17E-03	4.86E-03	8.26E-03	1.38E-02	2.47E-02	-4.04E-02
Y-force	1.48E-03	3.18E-03	5.20E-03	7.87E-03	1.22E-02	1.96E-02	6.96E-02
Z-force	3.44E-01	3.45E-01	3.47E-01	3.51E-01	3.57E-01	3.68E-01	4.00E-01

(a) Forces in the radial direction

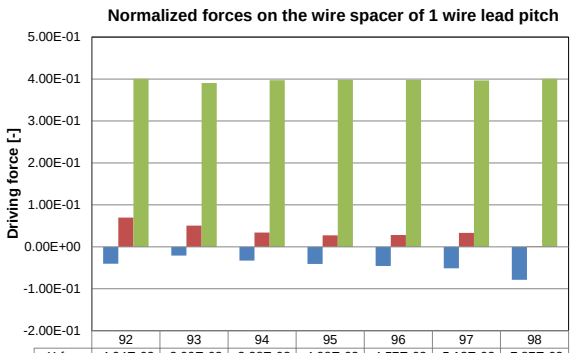

	92	93	94	95	96	97	98
X-force	-4.04E-02	-2.09E-02	-3.28E-02	-4.08E-02	-4.57E-02	-5.13E-02	-7.87E-02
Y-force	6.96E-02	5.04E-02	3.39E-02	2.73E-02	2.81E-02	3.33E-02	1.27E-03
Z-force	4.00E-01	3.91E-01	3.97E-01	3.98E-01	3.98E-01	3.97E-01	4.00E-01

(b) Forces in the tangential direction

Fig. 15. Normalized driving forces on the wire spacers in the radial and tangential directions

The driving forces in the X-, Y-, and Z-directions are not only dependent on the axial velocity, but also significantly dependent on the relative angular and relative position between the wire and duct wall. According to the investigation results of the driving forces on the wire-spacers, it is strongly recommended that the duct wall effect caused by the relative position of the wire and the duct should be considered in the edge and corner sub-channel analysis model (Ninokata at al. [20]].

4. Conclusions

The RANS based CFD methodology is evaluated with JAEA experimental data of the 127-pin wire-wrapped fuel assembly. Complicated and vortical flow phenomena in the wire-wrapped fuel bundles were elucidated. The conclusions are as below:

1. The RANS based CFD methodology has a good agreement with JAEA experimental data.
2. The edge vortex structures are longitudinally developed, and have a higher axial velocity than corner vortex structures and wakes nearby pins and wires. The wire spacers locally induce a tangential flow by up to about 16 % of the axial velocity. The tangential flow in the corner and edge sub-channels is much stronger than that in the interior sub-channels.
3. The large-scale edge vortex structures have higher turbulence intensity and lower vorticity than the small-scale wakes. The corner vortex structures have lower turbulence intensity and vorticity than the small-scale wakes.
4. The driving forces in the X-, Y-, and Z-directions are not only dependent on the axial velocity, but also significantly dependent on the angular position between the wire-spacer and rod, and the relative position between the wire-spacer and duct wall.

NOMENCLATURE

A	Angular position of wire spacer defined in eq. (5) [deg]
C_f	Friction factor constant defined in eq. (3) [-]

D_r	rod diameter [m]
D_w	wire diameter [m]
F	friction factor [-]
F_{25mm}	force acted on the wire of 25mm [N]
$F_{n,25mm}$	normalized F_{25mm} [N]
H	wire spacer lead pitch [m]
N	number of driving force integrating region per one wire-spacer lead pitch [-]
N_r	number of fuel pins [-]
P_t	rod pitch for wire-wrap configuration [m], = $D_r + 1.044 \times D_w$
Re	Reynolds number [-]
S_t	total wetted perimeter [m]
U	inlet velocity [m/s]
X	X coordinate [m]
Y	Y coordinate [m]
P	sodium density [kg/m^3]
γ	Intermittency factor [-]

SUBSCRIPTS

F	Denotes friction factor [-]
l, L	Denotes laminar flow region
t, T	Denotes turbulent flow region
in	Inlet

ACKNOWLEDGEMENTS

This work has been performed under the nuclear R&D program supported by the Ministry of Science, ICT and Future Planning of the Republic of Korea.

REFERENCES

[1] D.S. Rowe, COBRA Ⅲ-C: A digital computer program for steady state and transient thermal hydraulic analysis of nuclear fuel elements, Battle Pacific Northwest Laboratories, BNWL-1695, (1973).
[2] J.D. Macdougall, J.N. Lillington, The SABRE code for fuel rod cluster thermo-hydraulics, Nuclear Engineering and Design, 82, (1984), 171-190.
[3] H. Ninokata, ASFRE-Ⅲ: a computer program for triangular rod array thermo-hydraulic analysis of fast breeder reactors, PNC Report, PNC N941 85-106, (1985).
[4] W.S. Kim, Y.G. Kim, and Y.J. Kim, A subchannels analysis code MATRA-LMR for wire wrapped LMR subassembly, Annuals of Nuclear Energy, 29, (2002), 303-321.
[5] W.D. Pointer, P. Fischer, A. Siegel, and J. Smith, RANS-based CFD simulations of wire-wrapped fast reactor fuel assemblies, Proceedings of ICAPP '08, Anaheim, California, (2008).
[6] I. Ahmad, K.Y. Kim, Flow and convective heat transfer analysis using RANS for a wire-wrapped fuel assembly, Journal of Mechanical Science and Technology, 20, (2006), 1514-1524.
[7] R. Gajapathy, K. velusamy, P. Selvaraj, P. Chellapandi, and S.C. Chetal, CFD investigation of helical wire-wrapped 7-pin fuel bundle and the challenges in modeling full scale 217 pin bundle, Nuclear Engineering and Design, 237, (2007), 2332-2342.
[8] W. Raza, K.Y. Kim, Shape optimization of wire-wrapped fuel assembly using Kriging metamodeling technique, Nuclear Engineering and Design, 238, (2008), 1332-1341.
[9] W.D. Pointer, J.T. Tom, T. Fanning, P. Fischer, A. Siegel, J. Smith, and A. Tokuhiro, RANS-based CFD simulation of sodium fast reactor wire-wrapped pin bundles, Proceedings of International Conference on Mathematics, Computational Methods & Physics (M&C 2009), Saratoga Springs, New York.
[10] W.D. Pointer, P. Fischer, J. Smith, A. Obabko, and A. Siegel, Simulations of turbulent diffusion in wire-wrapped sodium fast reactor fuel assembly, Proceedings of International Conference on Fast Reactors and Associated Fuel Cycle, Kyoto, Japan, (2009).
[11] P.F. Fischer, A. Siegel, and P. Palmiotti, Large eddy simulation of wire wrapped fuel pins Ⅰ: Hydrodynamics in a periodic array, Proceedings of International Conference on Mathematics, Computational Methods & Physics (M&C 2007), Monterey, California.
[12] J.H. Jeong, J. Yoo, K.L. Lee, K.S. Ha, H.Y. Jeong, RANS based CFD methodology and challenge in modeling real scale 217-pin wire-wrapped fuel assembly of KAERI PGSFR, The 23rd International Conference on Nuclear Engineering, Chiba, Japan, ICONE23-1331, (2015).
[13] H. Narita, H. Ohshima, Improvement of Single-phase Subchannel Analysis Code ASFRE-III –Verification Analysis of Fuel Pin Heat Transfer Model and Pressure Loss Model, PNC TN9410 97-104, (2015).
[14] D. C. Wilcox, Reassessment of the Scale-determining Equation for Advanced Turbulence Models, AIAA Journal, 26(11), pp.1299-1310, (1998).
[15] F. R. Menter, Two-equation eddy-viscosity turbulence models for engineering applications, AIAA Journal, 32(8), pp. 1598-1605, (1994).
[16] K. Rehme, Pressure Drop Correlations for Fuel Element Spacers, Nuclear Technology, 17, (1973), 15-23,.
[17] F. C. Engel, R. A. Markley, and A. A. Bishop, Laminar, Transition, and Turbulent Parallel Flow Pressure Drop Across

Wire-wrap-spaced Rod Bundles, Nuclear science and engineering, 69, (1979), 290-296.
[18] S. K. Cheng and N. E. Todreas, Hydrodynamic Models and Correlations for Bara and Wire-wrapped Hexagonal Rod Bundles-bundle Friction Factors, Sub-channel Friction Factors and Mixing Parameters, Nuclear Engineering and Design, 92, (1986), 227-251.
[19] M. Fiebig P. Kallweit, and S. Tiggelbeck, Heat transfer enhancement and drag by longitudinal vortex generators in channel flow, Experimental Thermal and Fluid Science, 4, (1991), 103-114.
[20] H. Ninokata, A. Efthimiadis, and N. E. Todreas, Distributed resistance modeling of wire-wrapped rod bundles, Nuclear Engineering and Design, 104, (1987), 93-102.